AGU PUBLICATIONS

JGR

Journal of Geophysical Research: Solid Earth

RESEARCH ARTICLE
10.1002/2016JB013915

Key Points:
- Evidence for a northeastward dipping, slab-like seismic anomaly within the top of the lower mantle below the central United States
- The seismic waveforms recorded with the dense USArray show multipathing indicative of sharp top and bottom surfaces of the imaged slab
- Plate tectonic reconstructions suggest strong coupling of the Farallon Slab to North America Plate

Supporting Information:
- Supporting Information S1

Correspondence to:
D. Sun,
sdy2014@ustc.edu.cn

Citation:
Sun, D., M. Gurnis, J. Saleeby, and D. Helmberger (2017), A dipping, thick segment of the Farallon Slab beneath central U.S., *J. Geophys. Res. Solid Earth*, *122*, 2911–2928, doi:10.1002/2016JB013915.

Received 29 DEC 2016
Accepted 25 MAR 2017
Accepted article online 28 MAR 2017
Published online 20 APR 2017

A dipping, thick segment of the Farallon Slab beneath central U.S.

Daoyuan Sun[1,2], Michael Gurnis[3,4], Jason Saleeby[4], and Don Helmberger[3,4]

[1]Laboratory of Seismology and Physics of Earth's Interior & School of Earth and Space Sciences, University of Science and Technology of China, Hefei, China, [2]National Geophysics Observatory at Mengcheng, University of Science and Technology of China, Anhui, China, [3]Seismological Laboratory, California Institute of Technology, Pasadena, California, USA, [4]Division of Geological and Planetary Sciences, California Institute of Technology, Pasadena, California, USA

Abstract It has been hypothesized that much of the crustal deformation attributed to the Laramide orogeny of the southwest North American Cordillera was caused by dynamic effects induced by the flat subduction of a large oceanic plateau that was embedded within the Farallon Plate. Previous studies have identified within the North American mantle a seismic velocity anomaly that plausibly represents the remnants of the subducted plateau. Coupled plate kinematic and dynamic modeling of the anomaly, as well as surface geological findings, identify this anomaly as the subducted conjugate to the Shatsky Rise. Here we find clear evidence for a northeastward dipping (35° dip), thick (up to 400 km thick) slab-like seismic velocity anomaly within the top of the lower mantle below the central United States. Using a deep focus earthquake below Spain, we find that the observed seismic waveforms recorded with the dense USArray display multipathing indicative of sharp surfaces. Plate tectonic reconstructions in which the anomaly is migrated back in time suggest strong coupling of the plateau-thickened slab segment to the overriding North America Plate as it was subducted. In combination with the reconstructions, we interpret the structure as arising from eastward dipping Farallon subduction at the western margin of North America during the Cretaceous, in contrast with some recent interpretations. It appears that the plateau area of the slab has been further thickened, which might undergo a combination of pure shear bulk shortening during flat-slab subduction and/or by a folding instability during penetration into the lower mantle.

1. Introduction

Seismic tomography has had considerable success globally in the detection of high-velocity anomalies in the lower mantle that are compatible with the history of subduction from plate-tectonic reconstructions. A striking high-velocity anomaly, interpreted as the subducted Farallon Slab, has been imaged beneath North America [*Grand et al.,* 1997]. Although such imaging has revealed a broad N-S feature running from northwest Canada to central America, its 3-D shape displayed in tomographic models indicates a complex structure further implying a complicated subduction history [*Grand*, 2002; *Li et al*., 2008, 2014; *Ren et al*., 2007; *Sigloch*, 2011; *Simmons et al*., 2012, 2015; *van der Meer et al*., 2010]. The subducted Farallon Slab had a strong impact on the surface geology of the North America Plate, accented by the Laramide orogeny [*Liu et al*., 2010; *Spasojevic et al*., 2009], which deformed both the outer mobile belt and adjacent craton of southwest North America in the Late Cretaceous.

The Laramide Slab was apparently segmented into a shallow flat segment in the Southern California region and a deeper segment to the north to match the temporal evolution and geographic focusing of Laramide deformation during the latest Cretaceous to early Paleogene (Figure 1a) [*Saleeby*, 2003]. The shallow flat segment may have been caused by the relative buoyancy contrast resulting from the thickened and positively buoyant crust of the subducted oceanic plateau. *Saleeby* [2003] identifies the conjugate massif as the Shatsky Rise of the western Pacific Ocean basin that was embedded within the Farallon Plate during the Cretaceous as the subducted plateau. The existence of a conjugate massif to the Shatsky Rise is based on submarine observations of a rift edge with transform offsets along the eastern margin of the Shatsky Rise and a limited range of igneous construction ages for the Rise that are comparable to those of the underlying 140 Ma abyssal crust [*Sager*, 2005, and references therein]. These plate kinematic arguments are further supported by the discovery of pelagic limestone blocks within the Late Cretaceous Franciscan accretionary belt of California that closely match drilled and cored pelagic limestone beds that cap the Shatsky Rise [*Vallier et al*., 1983; *Sliter*, 1984]. Although the profound conditions that drove petrogenesis of the Shatsky Rise

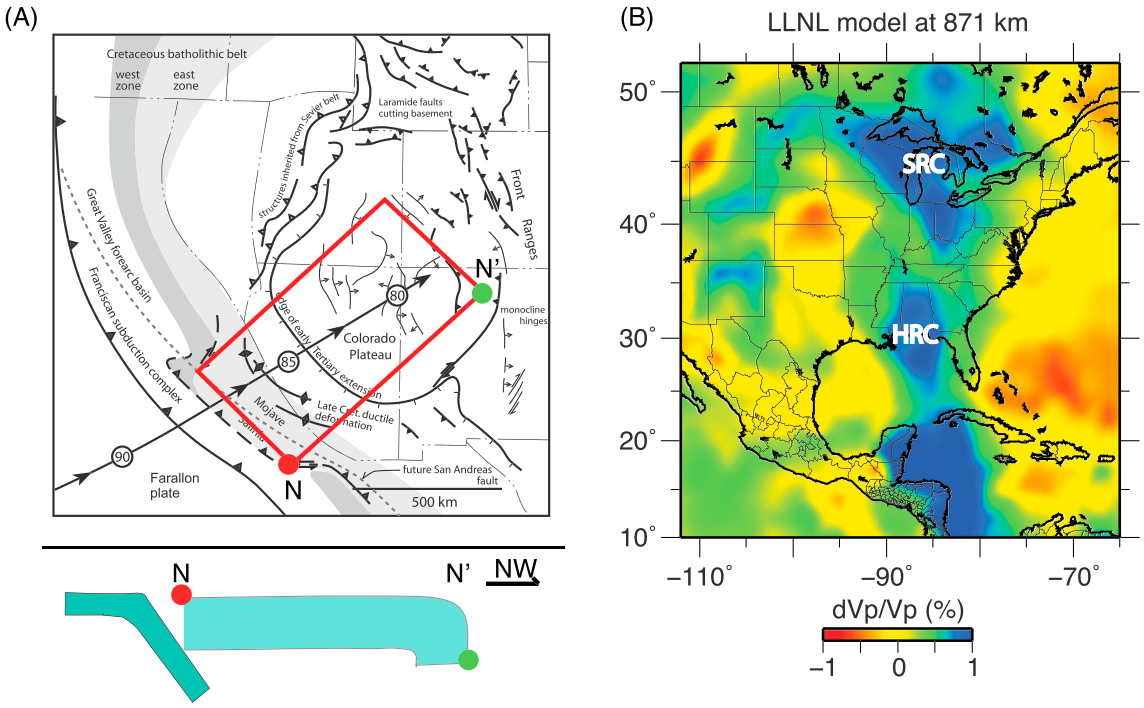

Figure 1. Tomography image of the Farallon Slab for the middle mantle and geological features related to the flat subduction. (a) Location of the flat slab at 70 Ma. The red rectangle represents the flat slab portion inferred from *Saleeby* [2003]. The bottom cartoon displays the subduction scenario at 70 Ma, when the thick flat slab NN′ broke away from the newly developed dipping subduction. Circles with number represent the volumetric center of the Shatsky Rise conjugate plateau at given age. The arrows indicate the subduction direction. (b) LLNL-G3Dv3 model [*Simmons et al.*, 2012] at the depth of 871 km, with three dominant blue patches. The most southern patch beneath the Caribbean is expected from normal slab fall. The middle one (HRC) beneath the northern edge of the Gulf of Mexico could be associated with Hess Rise conjugate, while the northern patch (SRC) appears to be dipping to the NE, perhaps the Shatsky Rise conjugate.

basalts are still under discussion, the up to ~35 km of mid-ocean ridge basalt crust that forms the rise indicates rapid igneous construction with high melt productivity [*Korenaga and Sager*, 2012]. This in turn requires a much greater thickness of depleted peridotite below the rise than typical oceanic lithosphere [*Sano et al.*, 2012]. Such a thick peridotite residue, depleted of volatile components, would in turn form a thick high-viscosity keel upon thermal relaxation and promote a thickened mantle lithosphere, relative to that of the adjacent ocean floor. In short, assuming that the Shatsky Rise Conjugate (SRC) approximated a mirror image to the currently observed Shatsky Rise, the conjugate likely possessed a thickened basaltic crust as well as thickened depleted uppermost mantle lithosphere. The composited effect may produce the positive buoyance leading to flat subduction.

The depth distribution of the high-velocity anomalies in global tomographic models corroborates the existence of flattened segments within the Farallon Slab. That is, the seismic anomalies around the Pacific Ocean near the core-mantle boundary align with their predicted positions if the subducted slabs sink vertically at a rate of 1 to 1.5 cm/yr on average [*Grand et al.*, 1997; *van der Meer et al.*, 2010]. Based on the above hypothesis, some high-velocity structures at the top of the lower mantle beneath the eastern United States appear to be too shallow if they are not connected to present subduction (Figure 1b). In this case the delayed descent of the Farallon Slab is used as evidence for a possible hiatus caused by a period of flat-slab subduction starting at Late Cretaceous [*Spasojevic et al.*, 2009] along the West Coast of the U.S. Present-day evidence of the subduction of the Cocos Plate beneath central America indicates that it underplates the continental crust and is effectively decoupled by a thin ultralow-velocity zone [*Song et al.*, 2009]. This flat slab drops sharply into the mantle near Mexico City where the surface elevation increases abruptly [*Perez-Campos et al.*, 2008]. Such behavior is compatible with the topology of the subducted slab of the much older Laramide orogeny hypothesized by *Saleeby* [2003] except in smaller dimensions.

By combining plate kinematic reconstructions and inverse mantle convection models, *Liu et al.* [2010] demonstrated the plausibility of the SRC having collided and subducted beneath the Southern California segment of the Cordilleran convergent margin in the Late Cretaceous, commencing at circa 90 Ma (Figure 1a).

The predicted location of initial collision of the Shatsky Rise with North America corresponds to a segment of the Cordilleran margin that underwent a distinct focused phase of shallow flat subduction and orogenic deformation initiating at circa 90 Ma, the red block in Figure 1a. This deformation regime can be linked to the initiation of classic Laramide structures of the Cordilleran interior. In particular, *Liu et al.* [2010] explored the dynamic effects of such a shallow flat slab segment on vertical displacements induced by dynamic topography, which were linked to the marine inundation evident through the Cretaceous Interior Seaway and the migration of the depocenters within the seaway.

The recognition of the eastward dipping Farallon Slab at depth is based on tomographic models [*Bijwaard et al*., 1998; *Grand*, 2002; *Schmid et al*., 2002; *Li et al*., 2008; *Porritt et al*., 2014; *Ren et al*., 2007; *Schmandt and Lin*, 2014; *Simmons et al*., 2012; *van der Meer et al*., 2010] but with limited resolutions and smeared boundaries. With recently developed methods, the tomographic images are becoming sharper. An example includes an updated *P* wave model, LLNL-G3Dv3 [*Simmons et al*., 2012], which appears to favor a structure that dips eastward (Figure 2a). An earlier image along this same corridor is presented in Figure 3a for comparison. The LLNL-G3Dv3 model involves adding horizontal paths, *Pn* arrivals, as well as using refined locations by applying a global multiple-event locator. Moreover, this new method applies 3-D ray tracing involving undulating interfaces to better resolve shallow fine structure [*Simmons et al*., 2012]. *Sigloch* [2011] developed a model including frequency-dependent traveltime corrections (Figure 2b). Figure 2 displays the two models at three different azimuths and shows a number of similarities including the eastward dipping nature of the seismic structure (Figure 2). An updated model LLNL-G3D-JPS [*Simmons et al*., 2015] shows similar features (Figure S1 in the supporting information). This eastward dipping nature is also clearly imaged in model UU-P07 [*van der Meer et al*., 2010] which is also based on a variety of *P* wave data derived from precise earthquake location.

However, the smearing images of the early tomographic models have been sufficiently ambiguous to allow for different interpretations of the subduction history. The eastward dipping Farallon Slab hypothesis [*Liu*, 2014; *Liu et al*., 2008] has been called into question with an alternative plate tectonic interpretation in that the seismic anomaly is approximated by a vertical wall that resulted from westward dipping, intraoceanic subduction of an oceanic plate attached to North America during the Cretaceous [*Sigloch and Mihalynuk*, 2013]. Thus, a waveform modeling study will be helpful in distinguishing between the two interpretations.

Here we exploit the dense USArray data and show that it is possible that the blurry tomographic image can be replaced with slab-like structures using waveform modeling. Moreover, we migrated this slab-like feature back in time to understand its plate-like structure and kinematic relations with the North American Plate (NAM), which are defined by the motion of the Farallon Plate (FAR) relative to the NAM with some period of docking, i.e., common motion or coupling.

2. Data

The waveform record sections used in this study were obtained from the USArray seismic network. In particular, the deep Spanish event (20100411, Table 1), studied by *Bezada and Humphreys* [2012] and *Buforn et al.* [2011] produced an excellent set of waveform data sampling the mantle structure along this corridor below the central and eastern United States (Figure 3). These waveforms were produced by first deconvolving the instrument response and then rotating them into transverse and radial components with a sample of *SH* waves displayed in Figure 3e. The data were band-passed filtered to 0.5–50 s.

We also used a shallow Atlantic ridge event (20091217) at a closer distance that does not display the diagnostic complexity (Figure S2). Later in section 3.4, we included data from two deep Fiji events 20110729 and 20120124 (Table 1) forming a reversed record section. If we hypothesize that the actual structure is slab like and dipping toward the east, then the raypath arrivals would be optimal for determining its sharpness, seismic velocity contrast, width, and depth [*Sun et al*., 2009; *Sun and Helmberger*, 2011].

3. Waveform Simulations

We will explore slab-like structures, which are consistent with structures evident in recent tomographic images (at azimuths 300° to 310° from the Spanish event, Figure 3), to explain the USArray data. For *S* waves passing through the traveltime-generated tomographic model TX2000 [*Grand*, 2002], we find a 4 s traveltime anomaly along with reduced amplitude as a function of distance (Figure 3b) with some apparent defocusing

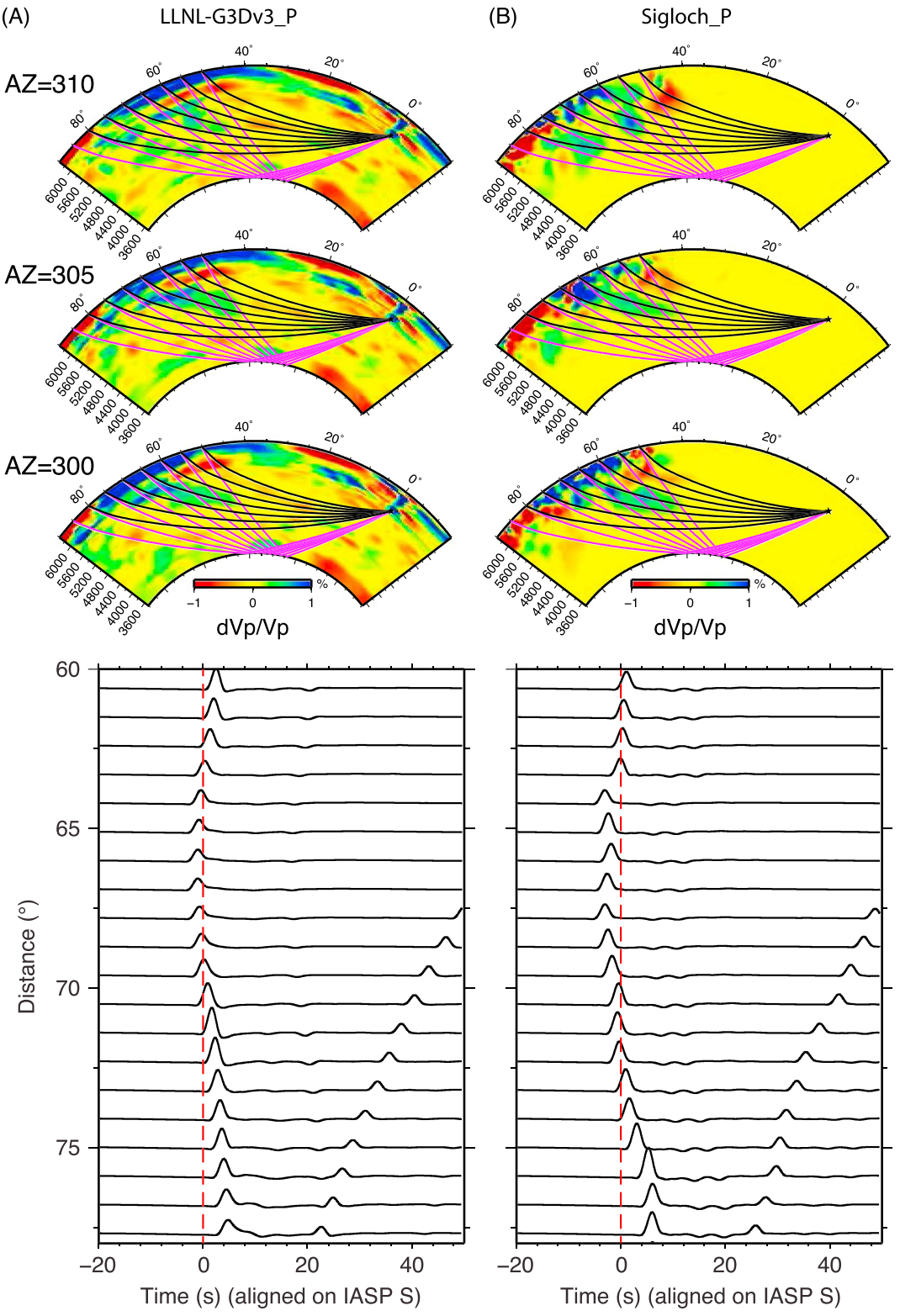

Figure 2. The 2-D cross sections through two different *P* tomography models and their predicted *SH* synthetics. The event is the 2010 deep Spain earthquake (Table 1). (a) LLNL-G3Dv3 model and (b) *Sigloch*'s [2011] model. The bottom row is the predicted SH synthetics by multiplying the *P* velocity perturbation by 2 for the azimuth of 305°.

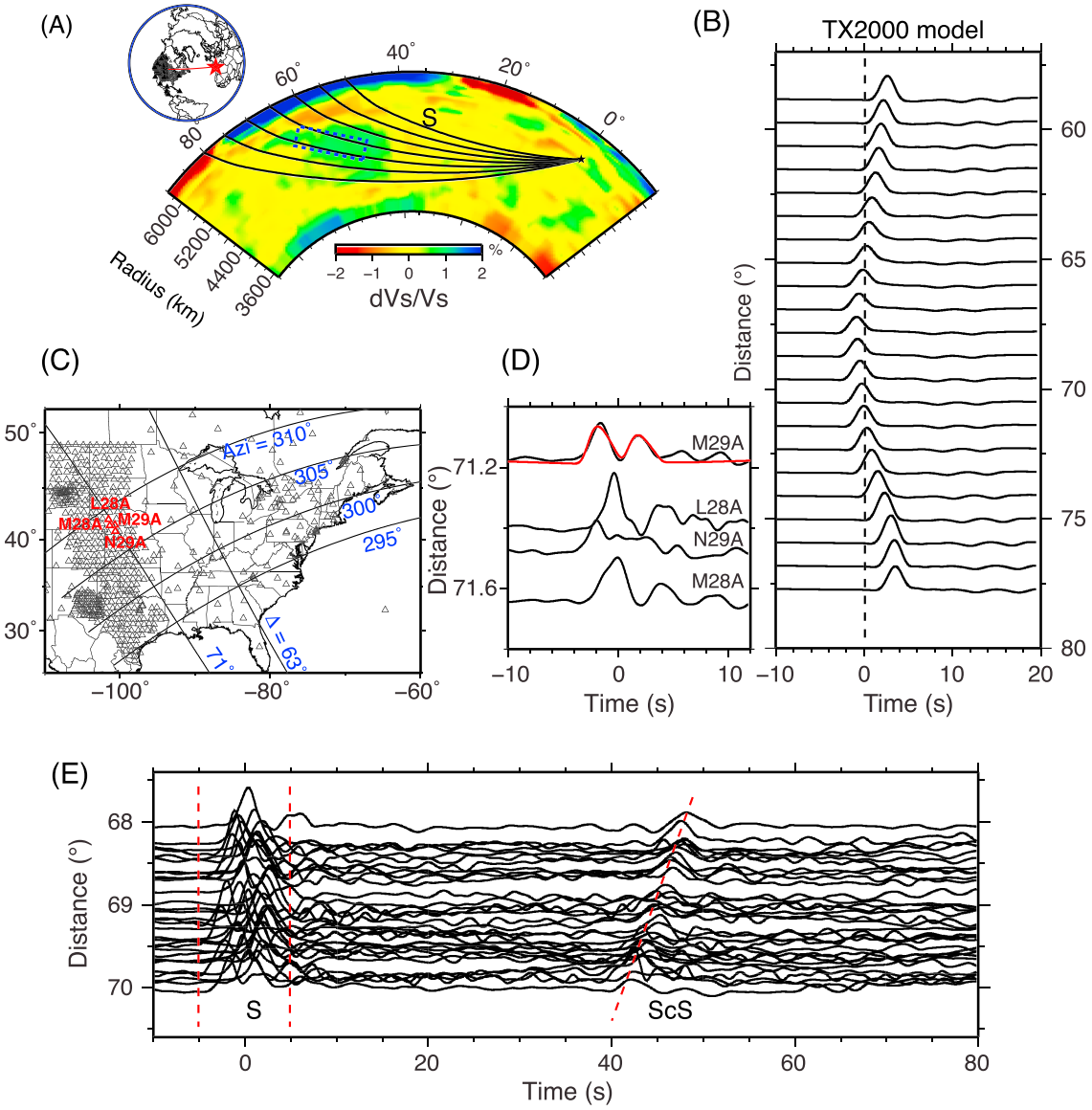

Figure 3. (a) The 2-D cross section through shear wave tomography model TX2000 [*Grand*, 2002] along a great circle between the 2010 deep Spain earthquake (Table 1) and the USArray. Black lines are the raypaths for the *S* phase. The blue dashed rectangle illustrates the putative slab. (b) *S* arrivals predicted from the tomography model in Figure 3a. Stations used in the analysis are plotted in Figure 3c. (d) Individual *S* records for neighboring stations in Nebraska (labeled in red in Figure 3c), which have strong waveform changes for the small spatial intervals among USArray stations. The red seismogram displays a simulated waveform from the multipath detector (MPD) analysis. (e) An example section of *SH* data, with strong variation between first *S* arrivals but less between *ScS* arrivals.

effect. These synthetics were generated with an analytical method, WKBJ modified (WKM) [*Ni et al.*, 2000]. The WKM method, specifically developed to construct synthetics from tomographic models [*Ni et al.*, 2000], has been validated against full numerical solutions of the seismic wave equation in 2-D and 3-D [*Li et al.*, 2014]. These codes produce similar seismograms unless sharp features are present in which case a full solution with finite difference synthetics are preferred, as shown through a comparison with regional synthetic seismograms [*Chu et al.*, 2012a].

Table 1. Earthquakes Used in This Study

Event	Date	Latitude (deg)	Longitude (deg)	Depth (km)
1	2010/04/11	37.10	−3.69	616
2	2009/12/17	36.47	−9.89	48
3	2011/07/29	−23.78	179.92	539
4	2012/01/24	−25.00	178.72	582

We find that the synthetics generated from the tomographic models

vary smoothly (Figures 2 and 3, while the observed waveforms and traveltimes vary rapidly near 69°. In particular, the *S* arrivals change from early to normal with distance increasing while showing extreme changes in waveform complexity from 68° to 70° (Figure 3e). In contrast, in this distance range the record section shows much less variation in *ScS* (Figures 3e and S3).

To distinguish between smooth and sharp features requires detailed comparisons across short-distance ranges (Figures 3c and 3d) as illustrated by four neighboring stations located in central Nebraska (Figure 3c), a region of simple crustal structure. Recordings from regional earthquakes at these same stations, for example, a Quebec event arriving along the same azimuth, are well modeled with simple upper mantle structures [*Chu et al*., 2012b]. Furthermore, waveforms from a shallow Atlantic event at these same stations are relatively well behaved (Figure S2). In short, we suppose that most of these complex waveforms (Figure 3e) are caused by multipathing involving a fast path inside the slab and a slower path just outside the slab with differential traveltimes of over 4 s.

We focus on defining the slab structure by using a combination of waveform patterns and traveltimes across the USArray, which we present in the next three sections. We first discuss the multipathing detector analysis (section 3.1), which allows us to outline the edges of sharp mantle structures. We then present a large-scale perspective in which stacked record sections are compared with simple geometric slab descriptions, i.e., rectangles, to understand the sensitivities of seismic waveforms on slab sharpness (section 3.2). We follow by modeling each individual record, which is used as a basis for generating an idealized 3-D image of the slab (section 3.3). Finally, we verify the proposed slab model by using other events that transect the Farallon Slab with rays coming in reversed direction (section 3.4).

3.1. Multipath Detector Analysis and Stacking

The Multipath Detector (MPD) was developed to examine the waveform complexities across a dense seismic array systematically [*Sun et al*., 2009; *Sun and Helmberger*, 2011]. The complexities in the waveforms are commonly indicative of multipathing effects, including in-plane and out-plane multipathing, which are used to map sharp structures in the mantle directly. The MPD method simulates each observed body waveform by performing a decomposition with $[S(t) + C \times S(t - \Delta_{LR})]/2$, where $S(t)$ is the synthetic for a reference model and typically has a simple pulse shape. The time separation (Δ_{LR}) and amplitude ratio (C) are determined by obtaining a best cross correlation (typically with cross-correlation coefficient larger than 0.85) between a simulated waveform and the data. The traveltime of the composite waveform relative to the reference model synthetic is then defined as Δ_T, which is similar to traveltime measurements in conventional tomography but with more accuracy for complex waveforms. The Δ_{LR} describes the waveform complexity. Multipathing with larger values of Δ_{LR} produces more distorted waveforms. Although more complete calculations can be made through the addition of diffracted arrivals, most of the distortions can be tracked with this simple approach (Figure 4). Generally, the complexities observed on the *SH* component are also on the *SV* component as well (Figure S4) where the four stations L28A, M28A, M29A, and N29A display substantial differences observed on both components (Figure 3d), for which stations L28A and M28A have delayed arrivals and sharper waveforms and stations M29A and N29A display complex and weaker arrivals. The *P* waveforms also display such complexity (Figure S2). With maps of Δ_{LR} values (Figure 5), we can easily recognize features with high- or low-velocity anomalies and define their sharp edges. Using both *SH* and *SV* data, the Δ_{LR} maps are quite consistent with relatively strong Δ_{LR} delays between 63° and 71° where the first arrivals beneath Nebraska and South Dakota near 70°, roughly from azimuth 303° to 313°, are distinctly early (Figure 5). Synthetics generated from new tomographic models [*Sigloch*, 2011; *Simmons et al*., 2012] predict the location of this particular boundary well (Figure 2), but not the multipathing. The Δ_{LR} patterns for *SH* and *SV* are slightly different with *SV* somewhat stronger. In this case, the SV is stronger than SH due to the radiation pattern. However, both sets of signals display early arrivals when they are strongly multipathed, an expected behavior from a fast slab edge [*Sun and Helmberger*, 2011]. Thus, large anomalies in Δ_T and Δ_{LR} can be used directly to enhance the structural image (Figure 5, third column) where they form a particularly strong pattern (blue color) between the azimuths 307° and 315°. Note that such patterns are similar to those generated synthetically for both 2-D and 3-D models of slab structure [*Sun and Helmberger*, 2011].

All the waveforms were processed with the above MPD with the timing Δ_T plotted relative to AK135 [*Kennett et al*., 1995]. The traveltimes display considerable scatter especially at ranges 54° to 60° and

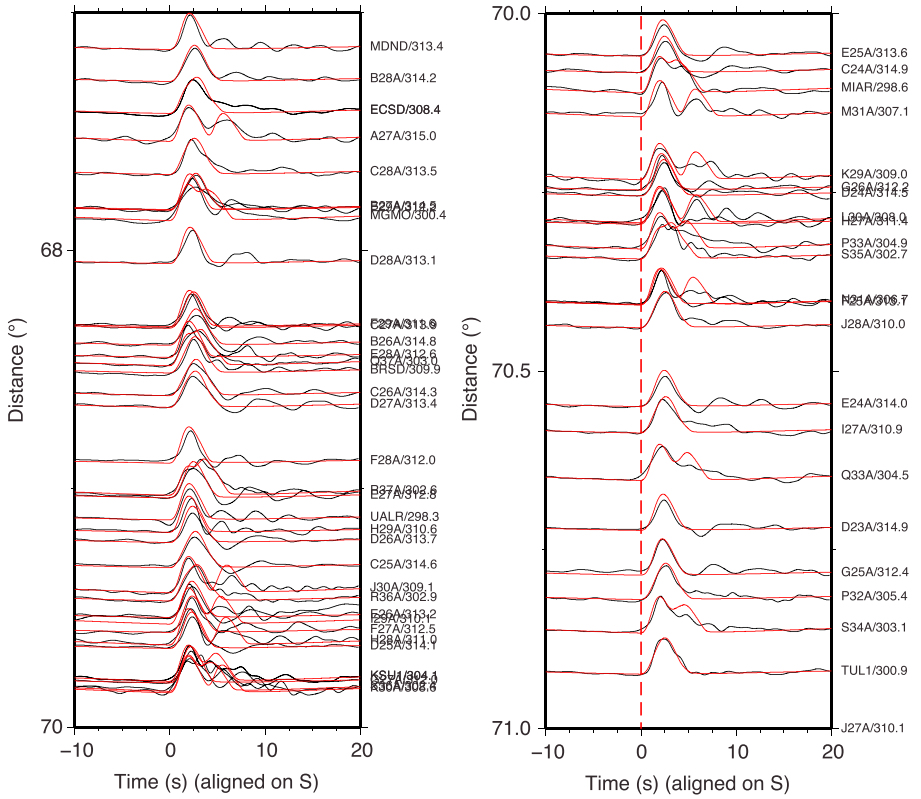

Figure 4. Examples of data (black) from the 2010 deep Spain earthquake and MPD simulations (red). The station name and azimuth are listed after every trace. In MPD simulation, a waveform data can be simulated by adding two synthetics with identical waveform generated from a reference model but allowing a time shift of Δ_{LR} between them. The Δ_{LR} are then determined by obtaining the highest cross-correlation coefficient (larger than 0.85) between a simulated waveform and the data. The more complicate waveform will have a larger value of Δ_{LR}.

beyond 68°, which are probably sampling the top and bottom edges of the slab structure. The data at the larger distances (>71°) display distinct azimuthal patterns where the waveforms to the north (azimuth of 315°–320°) arrive 2–3 s early (Figure 5a). A significant part of this feature may be associated with the Wyoming minicraton anomaly found in recent tomography [*Porritt et al.*, 2014; *Schmandt and Lin*, 2014]. The large-scale picture can be enhanced through the smoothing of these features by averaging or stacking the data.

We stack the data following a shift of every waveform into alignment with the average arrival times of Δ_T (Figure 6a, black line). The results for *SH* is given in Figure 6b displaying the raw displacement data (left), after correcting for timing to the average arrival times of Δ_T (middle), and after stacking (right). Much of the waveform complexity is removed with the 4 s anomaly clearly displayed with some complexity near 65° and 70° still apparent. The same procedure was repeated for the *SV* data (Figure S5) in which the *SKS* and *ScS* phases can be noted, even though the alignment chosen for stacking reduces their strength. The *P* waveforms are also consistent with the slab edges (Figure S6), but not as strong (Figure S2). Thus, we concentrate on the *SH* and *SV* record sections in a modeling exercise discussed next.

3.2. Model Constraints From Modeling Stacked Waveforms

Given such complexity, it becomes difficult to resolve the large number of parameters involved. We have attempted to simplify and concentrate on the main parameters: dip angle, width, and sharpness of the slab. Thus, as a first step we search for the general shape of the slab cross section and velocity contrast. Although we examined a large number of models, we discuss a few of the best models in this section with further examples given in the supporting information.

First, we investigate a slab with different dipping angles (Φ). The model with Φ of 30° produces strong diffraction arrivals from the slab edge for distances larger than 73°. When Φ is 40°, a second strong

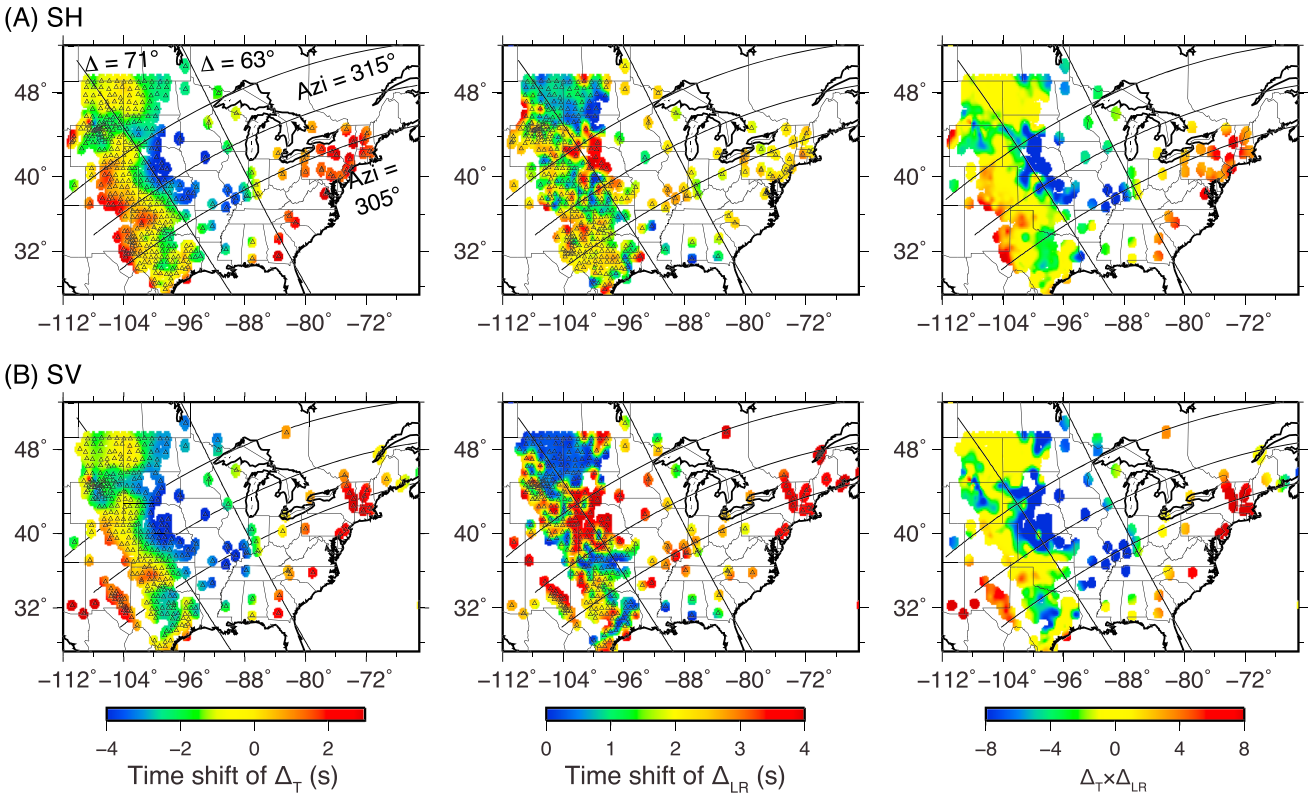

Figure 5. MPD patterns for (a) *SH* and (b) *SV* phases. From left to right: Traveltime anomaly (Δ_T), multipathing time separation (Δ_{LR}), and products of Δ_T and Δ_{LR}. The strong multipathing region (red color in Δ_{LR} map) associates with the earlier arrivals (blue color in Δ_T map) suggesting multipathing effects from a fast anomaly, i.e., lower mantle slab structure here. The product of Δ_T and Δ_{LR} further outlines the boundary of the slab structure.

arrival occurs at a distance of around 70° but the diffracted arrivals become weaker with increasing distance. The USArray data are best explained with a slab model with a dip angle of 35° (Figure 7). For simplicity, we fixed the dipping angles of 35° and only varied the width of the slab in the later modeling. We also truncate the small slab feature at the 660 km discontinuity since both regional modeling [*Chu et al.*, 2012b] and the LLNL-G3Dv3 model indicate simple upper mantle structure at this depth. The lower edge is less well defined but roughly compatible with the high-resolution tomographic models (Figure 2). We also investigated slabs that extend deeper, including one where the slab continues at constant dip (Figure S7b) and one which follows the raypaths (Figure S7c). In these cases, the velocity increase is assumed to be 2% with a 300 km slab thickness, which predicts considerable complexity near 70° not unlike that observed (Figure 3).

Next, we introduce some simple slab models and address geometric features (Figure 8). Here we attempt to fit both traveltimes and waveforms although the latter has been greatly smoothed by stacking. The best model fits are found with small time shifts and high cross correlations (Figure 8, first column). The best fitting model is compared against other models with larger-velocity anomalies and assorted shapes (Figure 8) along with cases assuming a range of geometries, including one case intended to represent the velocity variations associated with a slab that buckled before penetration into the lower mantle (Figure S8). We also examined the effects of adding transition zones along the slab edges (Figure S9). All these possible models can explain the general bulk properties of slab features and are not inconsistent with the original LLNL-G3Dv3 model tomographic image presented (Figure 2).

To produce a more detailed model fitting individual records, we will restrict the models to a 2% velocity increase (i.e., Figure 8, first column) along with the dip angle of 35°. We then allow each azimuthal strip to have different slab thicknesses while building a library of Green's functions (Figure 9). We will then generate a 3-D model of the slab by using this library to fit each individual observation.

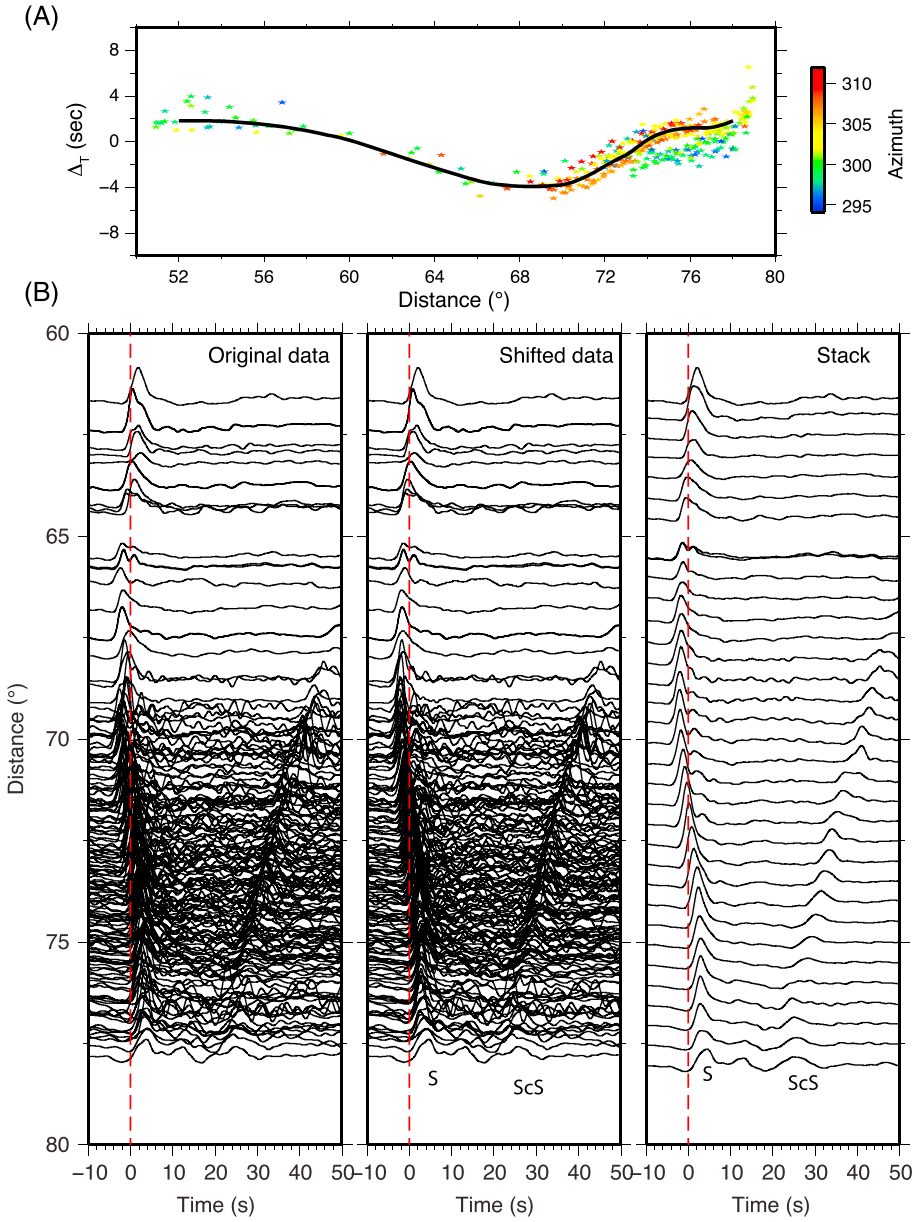

Figure 6. Data stacking procedure. (a) Measured traveltimes (Δ_T) from MPD analysis. Different colors denote the various different azimuths. The black line is a smoothed curve through the traveltimes. For distances large than 68°, only data with azimuths larger than 302° are used to generate the smoothed curve. (b) An example section of *SH* waveform data, where the left column is the original data. The middle column is the data shifted to the smoothed traveltime curve in Figure 6a. The right column is the stacked data for every 1° rolling over every 0.5°, where all traces are aligned on the predicted traveltimes for IASP model.

3.3. Hybrid Modeling

Here we suppose that each observed waveform is produced by an interference pattern containing multiple energy arrivals embedded in their Fresnel zones [*Helmberger and Ni*, 2005]. The difference between the right side of this energy packet and the left side causes multipathing as addressed earlier. This implies that if we examine a cluster of waveforms (e.g., Figure 3d), there should be a relationship between the arriving energy and the multipathing. That is, delayed arrivals should be sharper and strong (station L28), while early complex arrivals containing multipathing (station N29) should be weak. Such multipathing can be in the plane of propagation or out-of-plane (azimuthal). This type of relationship is adapted in our hybrid-modeling scheme (Figure 10). We can approximate these features by simply averaging neighboring synthetics either in-plane

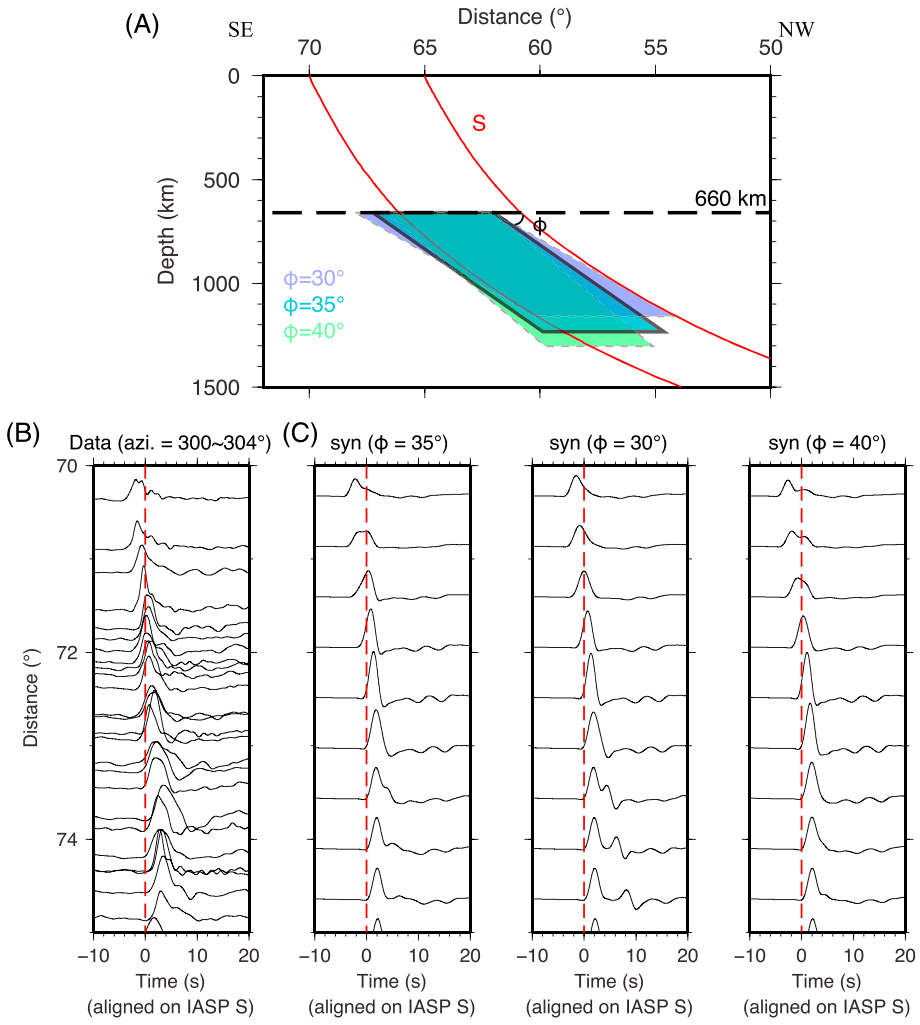

Figure 7. Sensitivity test of slab dipping angle (φ). (a) The top of the slab is fixed at the depth of 660 km and the slab thickness is 3°. The *S* velocity perturbation inside the slab is 2%. (c) Their synthetics. The model with φ of 35° predicts the data in (b) well in both waveform and amplitude better than the other two.

or out-of-plane, as discussed for higher-order diffracted contributions by *Song and Helmberger* [2006]. We display two synthetics, one with a thick slab (4°) and one with no slab (Figure 10a). The average of the two synthetics with different slab thickness provides a reasonable fit to the *SV* observation at the station L30A. Thus, we simulated every record with this approach. We first pick the synthetic from the library with different slab thickness (Figure 9) that best fits the first arrival (first dot) in timing for each individual record, denoted by a color dot of slab thickness at each station location (Figure 10c). The second arrival is chosen from a grid search involving 100 synthetic samples with the second dot of slab thickness indicating the best fit, derived from the highest cross-correlation coefficient (cc) between the composed synthetics with the observed waveform. Most of the fits have cc's larger than 0.9 (Figure S10). When a waveform is relatively long period, the two dots both have similar warm colors as in Figure 10c, indicating mostly radial in-plane multipathing. Most dots are red in the middle zone (thick slab) with more green (thin slab) in the northern section. Those stations displaying strong azimuthal behavior have two dots with strong contrast in colors. There are two zones displaying strong azimuthal multipathing. The northern edge displaying azimuthal multipathing is between region north and middle beneath Nebraska denoted by the dashed heavy blue line. A second zone occurs near the Oklahoma-Kansas border, the region between middle and southern but is less sharp. For the distances larger than 73°, all azimuths have a slab thickness of 4° (red color, Figure 10c). However, because the synthetics for all thicknesses are similar and the rays have passed the western edge of the slab (Figure 3a), this distance range is not ideal for resolving

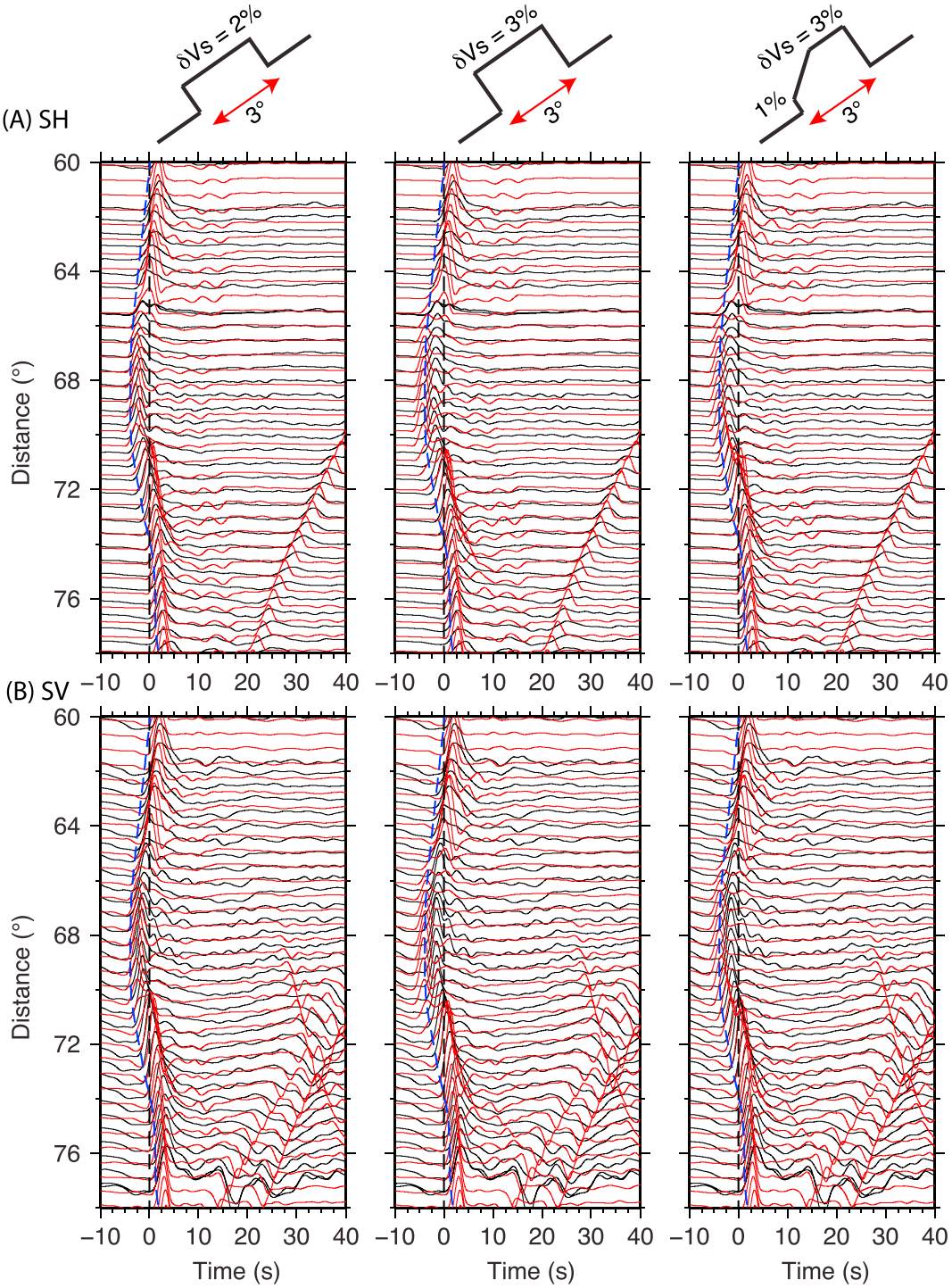

Figure 8. Predicted (a) *SH* and (b) *SV* for slab models with different velocity structures across the slab. Black traces are the data, and the red traces are the synthetics. Note that the deep structure effecting the core phases, *ScS* and *SKS*, is not addressed here although they are reasonably well matched. The blue dashed lines are the mean traveltimes curve from Figure 6a.

the slab thickness being sensitive to other features as discussed earlier. In summary, this matching of individual records of both *SH* and *SV* in timing and wave shape indicates that the middle portion (M) is thicker relative to the northern portion (N). In the next section we will produce evidence that validates this feature.

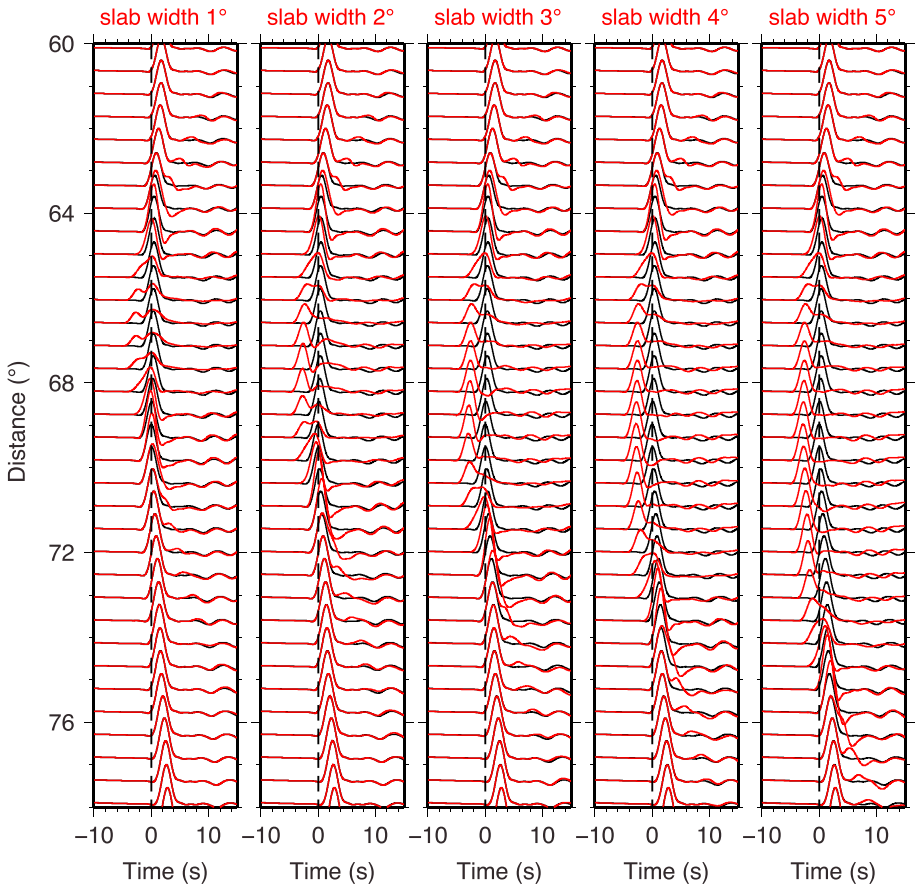

Figure 9. The synthetics (red traces) for models with different slab widths. The black traces are the synthetics for the model without the lower mantle slab.

3.4. Model Validation

Given increasing evidence for mantle complexity, it is difficult to sharpen images definitively unless we have a special set of paths like those presented above from the deep Spanish event. However, we can use our model to predict particular geometries where abrupt changes in the waveform might be observed (Figure 11). Our thickened-slab model at a depth of 940 km is presented in Figure 11a along with raypaths from a few examples of global deep seismicity. Paths in red correspond to sampling in a SE-NW direction from a South American event. The black raypaths display sampling from the reversed direction, NW to SE. Figure S11 displays the 2-D velocity sections along with raypath sampling the various anomalies from the NW Pacific region. Note that the thickened-slab feature from the northern source does not display much azimuthal difference that can be easily masked by other features. However, there is some sensitivity between azimuth of 335° to 340° from South American events (Figure S12). A better defined prediction is derived from the deep Fiji-Tonga events (Figure 11, green lines) where small changes in azimuth produces significant changes in the 2-D velocity cross sections, especially from the northern section to middle section (Figures 11c and 11d). Starting near 102° the thickened slab begins to speed-up observed *SKKS* as displayed (Figure 11c). Moreover, *SKS*, *SKKS*, and S_{diff} all speed-up at this range (Figure S13). However, as it appears that the *SKKS* is the least contaminated by other complications such as *SKPdS* and *SPdKS* in the *SKS* arrival, we will focus on *SKKS*. The reversal in the direction of arrivals obtained from the Fiji-Tonga event predicts a 2.5 s shift across the 46° to 50° northern edge (Figure 11d). Both waveforms and traveltimes appear to be affected starting near 102° where the thickened slab is first encountered. However, note that the top of the thickened slab model starts to the east of the Rocky Mountain Front and should be isolated from shallow structure (see Figure S14). Our predictions indicate a significant traveltime residual, supporting the westward shift of the Farallon Slab beneath the Midwestern U.S.

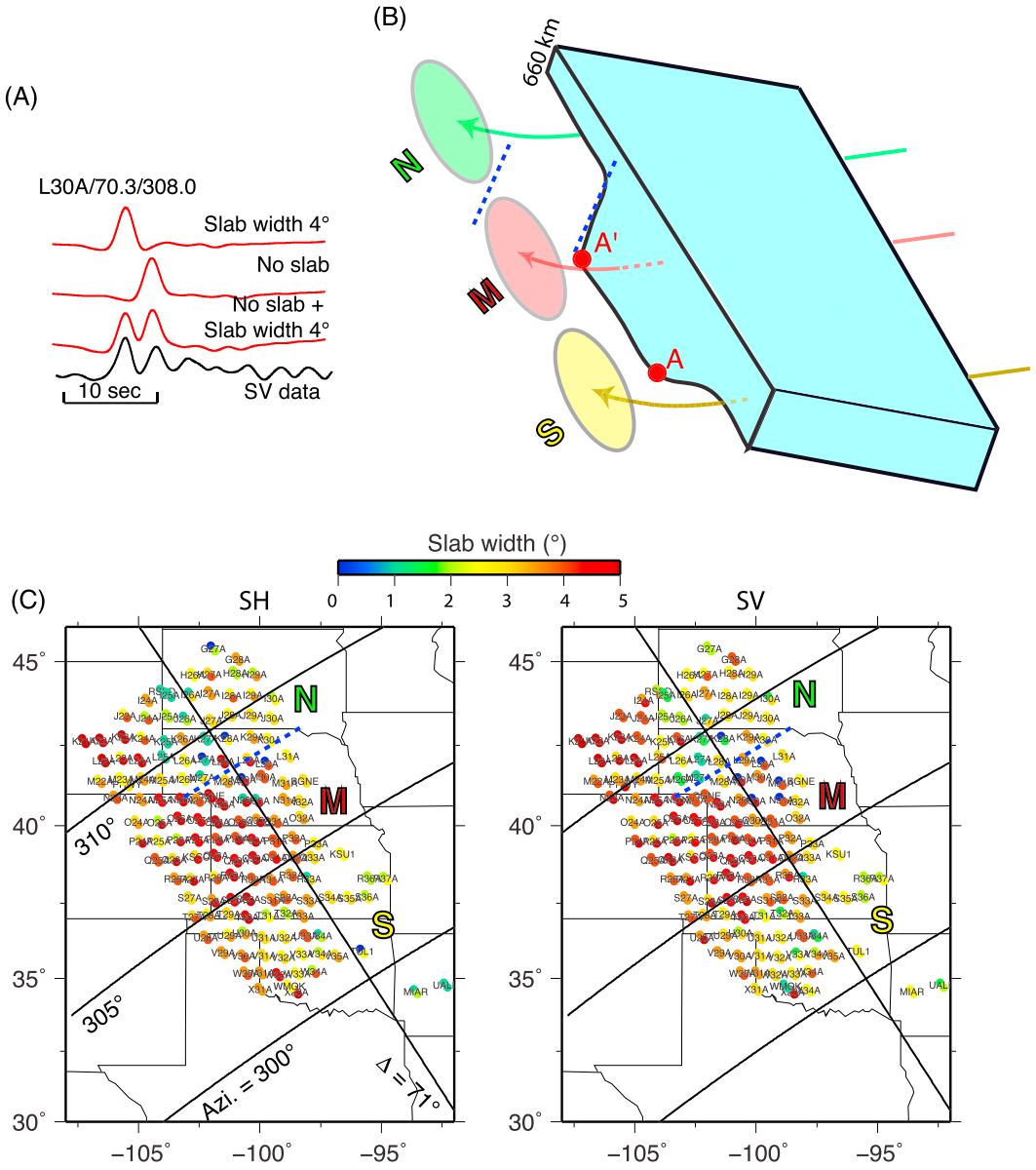

Figure 10. Lateral variations of the slab. (a) To capture the strong azimuthal multipathing, we assume that each seismogram is composed of two synthetics with different slab widths (Figure 9). (b) We model the thickened slab including northern (N), middle (M), and southern (S) parts having different thickness. Middle has the thickest mantle slab of 5°, while southern has a width of 3° and northern of 2°. The slab thickness changes abruptly from middle to northern, which causes strong azimuthal multipathing along such a boundary, indicated by the blue dash lines in Figure 10b. The inverted two thicknesses from Figure 10a for each station are plotted in Figure 10c with two circles next to the station for both *SH* (left) and *SV* (right); color coding indicates slab width. The stations with the most color contrast, i.e., blue (no slab) and red (slab width of 4°), indicating strong azimuthal multipathing, cluster along the boundary between patch northern and middle.

In the above analysis, we presented evidence for a major block (thickened-slab) dipping to the northeast with a strike of northern 45°E. Our results suggest considerable variation in thickness with a thickened slab in the middle dominating the anomaly. The northern segment is considerably thinner with a relatively sharp edge between block northern and middle. This feature agrees well with tomographic images presented (Figure 1b) and appears to be related to the northern edge of the red block outlined in Figure 1a. The southern segment is thicker than the northern and agrees with the

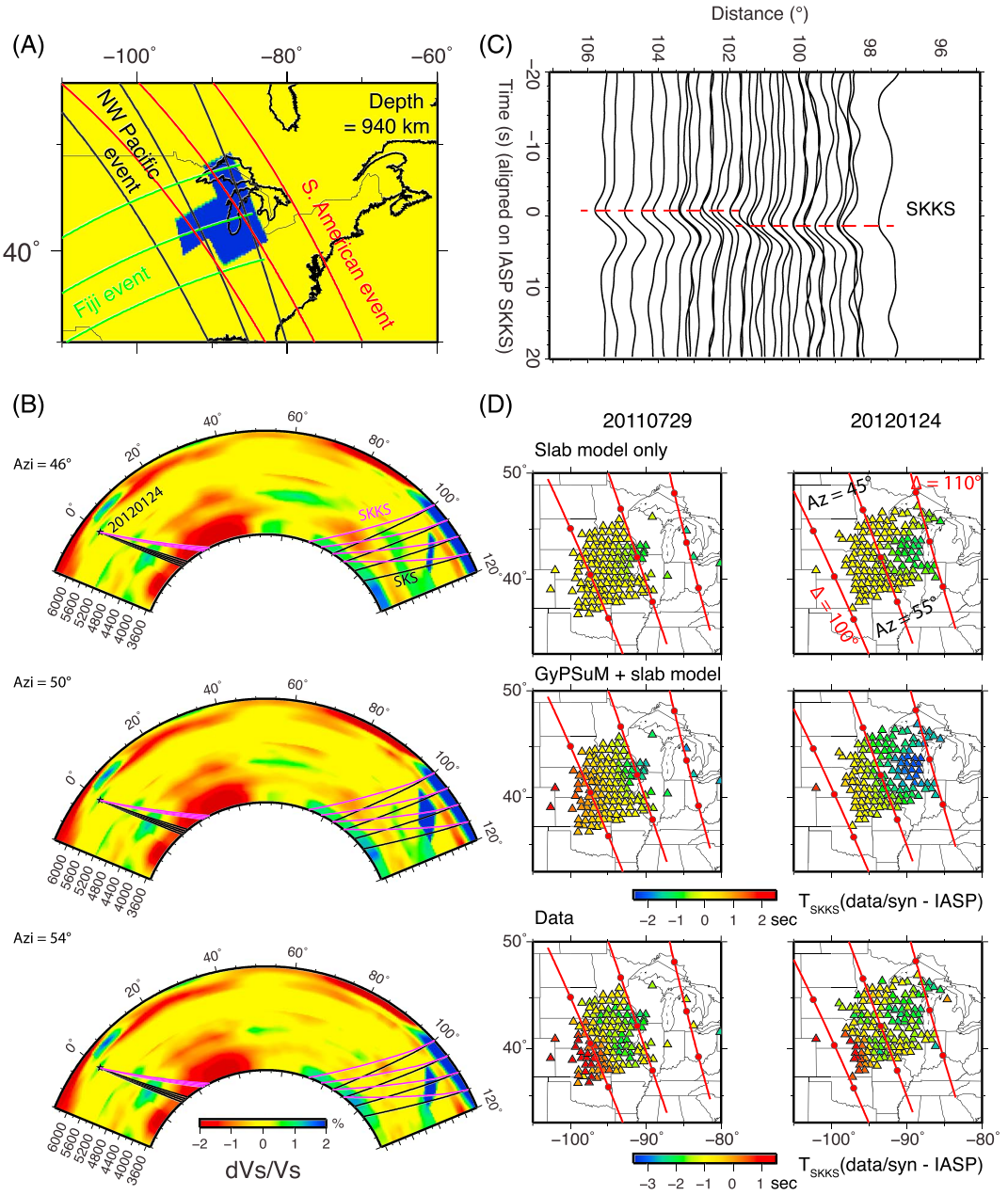

Figure 11. Predictions from the thickened slab model in Figure 10b. (a) The slab model (blue color) at the depth of 940 km. The lines with different colors display example raypaths sampling the thickened slab for events arriving from the NW Pacific (black), South America (red), and Fiji region (green). (b) The 2-D cross section through the GyPSuM model [*Simmons et al.*, 2010] substituted by the thickened slab at the depth of 660 to 1200 km along a great circle between an event at Fiji region and the USArray. The cross sections for events coming from other directions are displayed in Figures S11 and S12. (c) *SKKS* arrivals aligned on the AK135 [*Kennett et al.*, 1995] predicted traveltimes. Note the sharp traveltime jump at the distance of 101° with larger distance having faster arrivals. (d) The middle, thickest part (M) of the thickened slab predicts a patch with earlier *SKKS* arrivals (green colors) for both events in Fiji region. Adding the GyPSuM model enhances the traveltime contrasts (middle row) and explains the data well (bottom row).

tomographic image. Farther to the south (Figure 1b) is another significant anomaly referred to as the Hess Rise Conjugate (HRC) [see *Liu et al.*, 2010]. This structure is partially situated in the upper mantle and dips 50° to the southeast [*Ko et al.*, 2015]. In the next section, we evaluate the migration of the SRC through time relative to the North American and Farallon Plate.

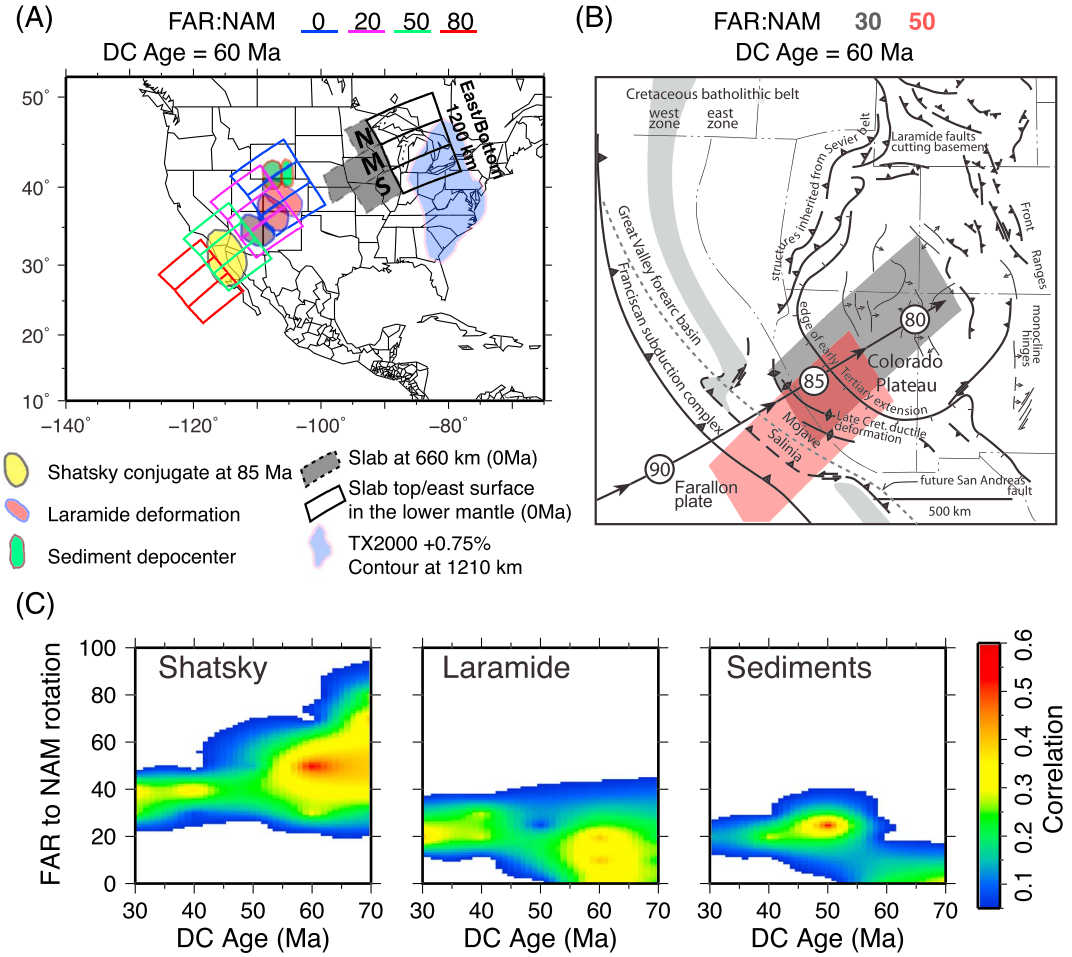

Figure 12. Reconstruction of the slab locations in a NAM plate frame of reference derived from rotations in *Seton et al.* [2012]. (a) Map with political boundaries, present-day slab locations in grey at the depth of 660 km, slab top surface, and slabs reconstructed to 85 Ma shown in color with a decoupling (DC) age of 60 Ma and for different FAR:NAM motions (0%, 20%, 50%, and 80%); 0% means the anomaly remains fixed to NAM, while 50% means that it was reconstructed with 50% of FAR rotation but the same pole with respect to NAM. (b) Palinspastic reconstruction of western U.S. shown with Laramide compressional structures [*Saleeby*, 2003] and reconstructed middle slab part at 80 Ma with DC age of 60 Ma and FAR:NAM motions of 30% (gray) and 50% (red). Arrowed line shows trajectory of the centroid of principal Shatsky Rise conjugate massif as it arrived and subducted with numbered circles denoting centroid location from 90 Ma to 80 Ma based on plate kinematic reconstruction in *Liu et al.* [2010]. Note westward breaching of eastern batholithic zone over flat slab segment resulting from Late Cretaceous extensional collapse across the trailing edge of conjugate massif as it subducted farther eastward. (c) Surface area correlation between the overlap of the middle portion and the Shatsky Rise conjugate at 85 Ma, Laramide deformation 85–75 Ma, and sediment depocenter at 80–75 Ma.

4. Plate Tectonic Correlations

Considering the plate tectonic and geological evolution of North America, what could such an east dipping, thickened lower mantle anomaly have originated from? Although the anomaly is much shallower and farther west than the seismic anomaly ascribed to Farallon Plate (FAR) subduction in past studies [*Bunge and Grand*, 2000; *Grand*, 2002] (Figure 3a), it is difficult to envision that an east dipping, volumetrically substantial anomaly is not related to east dipping subduction. The hypothesis that the east dipping anomaly resulted from west dipping subduction would require trench advance toward the west over hundreds of kilometers, a configuration that has not been found in either Cenozoic to recent plate tectonic reconstructions [*Seton et al.*, 2012] or in geodynamic models of subduction with self-consistent plate motions (see *Billen* [2008] for a review). Subduction of the Farallon Plate eastward below North America, including the geologically inferred period of the flat slab associated with the Laramide orogeny, is a plausible candidate for the east dipping slab. However, with thicknesses reaching 400 km, these

values are substantially larger than a thermal slab expected from the 30–50 Ma average age of the subducting Farallon Plate at Laramide time [*Seton et al*., 2012].

We use plate tectonic reconstructions to restore the putative Farallon Slab to its paleopositions under a wide range of parameters and correlated those restored positions with proxies for the position of the slab (Figure 1a). For the reconstructions, we rotated positions of the seismic anomalies computed with the rotations in *Seton et al*. [2012] using GPlates [*Boyden et al*., 2011] back in time. However, we do not know a priori how to restore the slab to the surface. As different parts of the restored slab may be responsible for different aspects of the geological history as addressed next, we used the six different seismic slab surfaces determined here and for comparison to older interpretations, the TX2000 seismic model [*Grand*, 2002] at 1210 km depth represented by the 0.75% contour of the seismic anomaly (Figure 12a). The six seismic slab surfaces (Figure 12a) correspond to the northern (N), middle (M), and southern (S) parts of the intersection of the anomaly with the 660 km discontinuity and the northern, middle, and southern faces of the anomaly with normal pointing upward toward the east.

We hypothesize that there were several phases in the motion between the mantle anomaly and the plates. During the first, and earliest phase (85 Ma to 140 Ma), the anomaly was attached to and rode passively with its primary FAR oceanic lithosphere. Here we introduce the age at which slabs become unattached to surface plate motions and became fixed in the lower mantle, the decoupling age (DC). During a second phase, earlier than this decoupling age, the anomaly was strongly coupled to NAM or FAR, with some combination of these two plate motions. This assumption would seem to encompass the wide range of possibilities that a slab could take while subducting through the upper mantle. Third, during the most recent phase, the anomaly is mechanically detached from the North American Plate (NAM) and is expected to sink relative to the deep mantle while NAM translated to the west during recent times. In geodynamic models with reasonable depth-dependent viscosity distributions [*Forte and Mitrovica*, 1996], thermal anomalies remain relatively fixed horizontally as plates and margins rapidly move [cf. *Zhong and Gurnis*, 1995], a concept which has been useful in correlating the location of ancient slab locations with lower mantle seismic anomalies [*Domeier et al*., 2016; *van der Meer et al*., 2010].

Earlier than the decoupling age the anomaly takes on motions intermediate between NAM and FAR. For intermediate values, we assumed the same pole positions but scaled angular rotations in proportion to a value of FAR:NAM, defined by the relative motion between NAM and FAR. A FAR:NAM motion of 0% means the anomaly remains fixed to NAM, while 50% means that it was reconstructed with 50% of FAR rotation but the same pole with respect to NAM. With higher value of FAR:NAM motion, FAR has weaker coupling with NAM; thus, FAR will move farther to the east relative to NAM with time advancing. If we migrated back the fixed current slab position, a slab position farther to the west will be expected for a higher value of FAR:NAM motion, i.e., weaker coupling (Figure 12a). There is an implied sinking velocity for each set of parameters. For a DC of 40 Ma, an average sinking rate (between the top of the anomaly at 660 km and its base at ~1250) of ~2 cm/yr is implied, not significantly inconsistent with geologically inferred values [*van der Meer et al*., 2010] and geodynamic models [*Bower et al*., 2013, Figure 10c]. The correlations were computed in the NAM frame of reference using GMT (http://gmt.soest.hawaii.edu/).

With two unknown parameters, DC and the proportion of FAR to NAM motion given to the anomaly, we find the correlation with three independent surface constraints thought to be indicative of regional subduction evolution. We use plausible outlines of the Shatsky Rise conjugate on FAR at 85 Ma which is long thought to be the trigger for the flat slab event [*Livaccari et al*., 1981]. We then use the mapped extent of the deformation zone in the SW part of the U.S., which migrated eastward from 85 to 75 Ma [*Saleeby*, 2003] (Figure 12b). This deformation has been interpreted as coupling between the subducting Farallon Slab and the overriding North American lithosphere. Finally, we use the migrating sediment depocenter that is thought to arise from the dynamic topography of the leading edge of the flat slab from 85 to 75 Ma [*Liu et al*., 2010, 2014]. As the slab, with some component of negative buoyancy, passed below the overriding plate it would have induced an eastward migrating dynamic subsidence. Essentially, as the slab is restored to the surface, the slab surface facing upward and toward the east would presumably have encountered shearing and coupling with the base of the North American lithosphere (Figure 12b). As we do not know how much the slab has rotated or deformed, we conservatively project the seismic outline of this face to the earth's surface.

We find that independent of decoupling age, the ratio of FAR to NAM must be small (Figure 12), implying that the motion of the anomaly was strongly coupled to NAM. Inference of a strong coupling is not sensitive to which geological proxy we correlated the rotated slabs with or which slab face we restore to the surface (Figures S15–S17). If such a relative motion between the two plates exists, the subducting plate could have undergone substantial internal deformation and thickening such that an originally ~80 km thick thermal slab would thicken to 200–400 km for ratios of FAR to NAM motion smaller than 50%. The thickening process could easily give rise to the requisite observed thicknesses and if the slab were purely thermal then a sharp top but not bottom would be expected. Alternatively, the thickening could have arisen from a folding instability as the slab enters the higher-viscosity lower mantle [*Gurnis and Hager*, 1988; *Griffiths and Turner*, 1988; *Ribe et al*., 2007; *Billen*, 2008]; however, this would give rise to oscillating edges to the anomaly that tend to suppress the multipathing (Figure S6). Consequently, there are several processes that can give rise to the magnitude of slab thickening inferred, but new geodynamic studies are now called for to simultaneously reconcile the sharp-sided eastward dipping slab with plate tectonic and geological constraints.

5. Conclusions

Seismic waveform records from the USArray for the deep, 2010 Spain earthquake sequence provide ideal raypaths sampling the high-velocity block beneath the U.S. Midwest at middle mantle depths. By detailed multipathing analysis and waveform modeling, we obtained two seismic observations defining this high-velocity block. First, this high-velocity anomaly is northeastward dipping (35° dip), which confirms its link to the eastward dipping Farallon subduction at the western margin of North America during the Cretaceous. Second, this thickened slab displays strong azimuthal variation in thickness. The thickest part is box like with a thickness of over 400 km. Given such a slab thickness and its location requires a complex displacement and strain history backward in time with plate tectonic reconstruction, which suggests strong coupling of the plateau-thickened slab segment to the overriding North America Plate as it was subducted. This result agrees with the existence of a flat subducting slab segment during the Late Cretaceous, when a distinctly thick block constituting the Shatsky Rise Conjugate (SRC) left a time transgressive deformation corridor from the Southern California convergent margin belt to the Colorado region foreland with dimensions of about 500 km in width and 1000 km in length [*Saleeby*, 2003]. Our plate tectonic reconstructions further suggest that the SRC essentially collided with and then subducted beneath the North American plate beginning at 85 to 90 Ma and proceeded to subduct eastward as a flat-slab segment for about 25 Ma, while it thickened by pure shear and/or folding before dropping into the mantle. Collision and initial subduction of the SRC correspond to well-documented flat-slab subduction features in the convergent margin belt, while subsequent partial coupling of the SRC to overriding North American lithosphere corresponds spatially and temporally to classic Laramide deformation of the Cordilleran interior. However, further geodynamic modeling with plate tectonic and geological constraints is needed to explain this observed eastward dipping FAR in the lower mantle.

Acknowledgments

The authors would like to thank the Editor Yehuda Ben-Zion, Associate Editor, Nathan Simmons, Jeroen Ritsema, Wim Spakman, and two anonymous reviewers. Their suggestions and comments were greatly appreciated and lead to significant improvements to the manuscript. Data are provided by IRIS data center and Earthscope USArray, which are available at http://www.iris.edu. All maps in this paper were produced using GMT developed by Paul Wessel and Walter H. F. Smith. D.S. supported by Strategic Priority Research Program (B) of Chinese Academy of Sciences, grant XDB18000000, the Fundamental Research Funds for the Central Universities in China WK2080000078, National Natural Science Foundation of China 41574037, and Key Research Program of Frontier Sciences CAS, grant QYZDB-SSW-SYS011. M.G. and D.V.H. supported by NSF grant EAR-1358646. Additional support for M.G. provided by NSF grant EAR-1247022.

References

Bezada, M. J., and E. D. Humphreys (2012), Contrasting rupture processes during the April 11, 2010 deep-focus earthquake beneath Granada, Spain, *Earth Planet. Sci. Lett.*, *353*, 38–46.

Bijwaard, H., W. Spakman, and E. R. Engdahl (1998), Closing the gap between regional and global travel time tomography, *J. Geophys. Res.*, *103*(B12), 30,055–30,078, doi:10.1029/98JB02467.

Billen, M. I. (2008), Modeling the dynamics of subducting slabs, *Annu. Rev. Earth Planet. Sci.*, *36*, 325–356.

Boyden, J. A., R. D. Müller, M. Gurnis, T. H. Torsvik, J. A. Clark, M. Turner, H. Ivey-Law, R. J. Watson, and J. S. Cannon (2011), Next-generation plate-tectonic reconstructions using GPlates, in *Geoinformatics: Cyberinfrastructure for the Solid Earth Sciences*, edited by G. R. Keller and C. Baru, pp. 44–63, Cambridge Univ. Press, Cambridge.

Bower, D., M. Gurnis, and M. Seton (2013), High bulk modulus structures in the lower mantle from dynamic earth models with paleogeography, *Geochem. Geophys. Geosyst.*, *14*, 44–63, doi:10.1029/2012GC004267.

Buforn, E., C. Pro, S. Cesca, A. Udias, and C. del Fresno (2011), The 2010 Granada, Spain, deep earthquake, *Bull. Seismol. Soc. Am.*, *101*(5), 2418–2430.

Bunge, H.-P., and S. P. Grand (2000), Mesozoic plate-motion history below the northeast Pacific Ocean from seismic images of the subducted Farallon Slab, *Nature*, *405*, 337–340, doi:10.1038/35012586.

Chu, R., B. Schmandt, and D. V. Helmberger (2012a), Juan de Fuca subduction zone from a mixture of tomography and waveform modeling, *J. Geophys. Res.*, *117*, B03304, doi:10.1029/2012JB009146.

Chu, R., B. Schmandt, and D. V. Helmberger (2012b), Upper mantle *P* velocity structure beneath the Midwestern United States derived from triplicated waveforms, *Geochem. Geophys. Geosyst.*, *13*, Q0AK04, doi:10.1029/2011GC003818.

Domeier, M., P. V. Doubrovine, T. H. Torsvik, W. Spakman, and A. L. Bull (2016), Global correlation of lower mantle structure and past subduction, *Geophys. Res. Lett.*, *43*, 4945–4953, doi:10.1002/2016GL068827.

Forte, A. M., and J. X. Mitrovica (1996), New inferences of mantle viscosity from joint inversion of long-wavelength mantle convection and post-glacial rebound data, *Geophys. Res. Lett.*, *23*(10), 1147–1150, doi:10.1029/96GL00964.

Grand, S. P. (2002), Mantle shear-wave tomography and the fate of subducted slabs, *Philos. Trans. R. Soc. London A*, *360*, 2475–2491.
Grand, S. P., R. D. Van der Hilst, and S. Widiyantoro (1997), High resolution global tomography: A snapshot of convection in the earth, *GSA Today*, *7*, 1–7.
Griffiths, R. W., and J. S. Turner (1988), Folding of viscous plumes impinging on a density or viscosity interface, *Geophys. J. Int.*, *95*(2), 397–419.
Gurnis, M., and B. H. Hager (1988), Controls of the structure of subducted slabs, *Nature*, *335*(6188), 317–321.
Helmberger, D. V., and S. Ni (2005), Approximate 3D body-wave synthetics for tomographic models, *Bull. Seismol. Soc. Am.*, *95*(1), 212–224, doi:10.1785/0120040004.
Kennett, B. L. N., E. R. Engdahl, and R. Buland (1995), Constraints on seismic velocities in the earth from travel times, *Geophys. J. Int.*, *122*, 108–124.
Ko, J., S. Hung, D. Li, and D. V. Helmberger (2015), The mantle seismic heterogeneities inferred by USArray data, Abstract DI51A-2612 presented at 2015 Fall Meeting, AGU, San Francisco, Calif., 14–18 Dec.
Korenaga, J., and W. W. Sager (2012), Seismic tomography of Shatsky Rise by adaptive importance sampling, *J. Geophys. Res.*, *117*, B08102, doi:10.1029/2012JB009248.
Li, C., R. D. van der Hilst, E. R. Engdahl, and S. Burdick (2008), A new global model for *P* wave speed variations in Earth's mantle, *Geochem. Geophys. Geosyst.*, *9*, Q05018, doi:10.1029/2007GC001806.
Li, D., D. Helmberger, R. W. Clayton, and D. Sun (2014), Global synthetic seismograms using a 2-D finite-difference method, *Geophys. J. Int.*, *197*(2), 1166–1183. doi: 10.1093/gji/ggu1050.
Liu, L. (2014), Constraining Cretaceous subduction polarity in eastern Pacific from seismic tomography and geodynamic modeling, *Geophys. Res. Lett.*, *41*, 8029–8036, doi:10.1002/2014GL061988.
Liu, L., M. Gurnis, M. Seton, J. Saleeby, R. D. Müller, and J. M. Jackson (2010), The role of oceanic plateau subduction in the Laramide orogeny, *Nat. Geosci.*, *3*, 353–357.
Liu, L., S. Spasojević, and M. Gurnis (2008), Reconstructing Farallon plate subduction beneath North America back to the Late Cretaceous, *Science*, *322*, 934–938.
Liu, S., D. Nummedal, and M. Gurnis (2014), Dynamic versus flexural controls of Late Cretaceous western interior basin, USA, *Earth Planet. Sci. Lett.*, *389*, 221–229.
Livaccari, R. F., K. Burke, and A. M. C. Sengor (1981), Was the Laramide orogeny related to subduction of an oceanic plateau, *Nature*, *289*(5795), 276–278.
Ni, S. D., X. M. Ding, and D. V. Helmberger (2000), Constructing synthetics from deep earth tomographic models, *Geophys. J. Int.*, *140*(1), 71–82, doi:10.1046/j.1365-246x.2000.00982.x.
Perez-Campos, X., Y. Kim, A. Husker, P. M. Davis, R. W. Clayton, A. Iglesias, J. F. Pacheco, S. K. Singh, V. C. Manea, and M. Gurnis (2008), Horizontal subduction and truncation of the Cocos Plate beneath central Mexico, *Geophys. Res. Lett.*, *35*, L18303, doi:10.1029/2008GL035127.
Porritt, R. W., R. M. Allen, and F. F. Pollitz (2014), Seismic imaging east of the Rocky Mountains with USArray, *Earth Planet. Sci. Lett.*, *402*, 16–25.
Ren, Y., E. Stutzmann, R. D. van der Hilst, and J. Besse (2007), Understanding seismic heterogeneities in the lower mantle beneath the Americas from seismic tomography and plate tectonic history, *J. Geophys. Res.*, *112*, B01302, doi:10.1029/2005JB004154.
Ribe, N. M., E. Stutzmann, Y. Ren, and R. D. Van der Hilst (2007), Buckling instabilities of subducted lithosphere beneath the transition zone, *Earth Planet. Sci. Lett.*, *254*, 173–179.
Sager, W. W. (2005), What built Shatsky Rise, a mantle plume or ride tectonics?, in Plates, Plumes, and Paradigms, *Geol. Soc. Spec. Pap.*, vol. 388, edited by G. R. Foulger et al., pp. 721–733, doi:10.1130/2005.2388(41).
Saleeby, J. (2003), Segmentation of the Laramide Slab—Evidence from the southern Sierra Nevada region, *Geol. Soc. Am. Bull.*, *115*, 655–668.
Sano, T., K. Shimizu, A. Ishikawa, R. Senda, Q. Chang, J.-I. Kimura, M. Widdowson, and W. W. Sager (2012), Variety and origin of magmas on Shatsky Rise, northwest Pacific Ocean, *Geochem. Geophys. Geosyst.*, *13*, Q08010, doi:10.1029/2012GC004235.
Schmid, C., S. Goes, S. van der Lee, and D. Giardini (2002), Fate of the Cenozoic Farallon Slab from a comparison of kinematic thermal modeling with tomographic images, *Earth Planet. Sci. Lett.*, *204*, 17–32.
Schmandt, B., and F.-C. Lin (2014), *P* and *S* wave tomography of the mantle beneath the United States, *Geophys. Res. Lett.*, *41*, 6342–6349, doi:10.1002/2014gl061231.
Seton, M., et al. (2012), Global continental and ocean basin reconstructions since 200 Ma, *Earth Sci. Rev.*, *113*(3–4), 212–270.
Sigloch, K. (2011), Mantle provinces under North America from multi-frequency *P*-wave tomography, *Geochem. Geophys. Geosyst.*, *12*, Q02W08, doi:10.1029/2010GC003421.
Sigloch, K., and M. G. Mihalynuk (2013), Intra-oceanic subduction shaped the assembly of Cordilleran North America, *Nature*, *496*, 50–56, doi:10.1038/nature12019.
Simmons, N. A., A. M. Forte, L. Boschi, and S. P. Grand (2010), GyPSuM: A joint tomographic model of mantle density and seismic wave speeds, *J. Geophys. Res.*, *115*, B12310, doi:10.1029/2010JB007631.
Simmons, N. A., S. C. Myers, G. Johannesson, and E. Matzel (2012), LLNL-G3Dv3: Global *P* wave tomography model for improved regional and teleseismic travel time prediction, *J. Geophys. Res.*, *117*, B10302, doi:10.1029/2012JB009525.
Simmons, N. A., S. C. Myers, G. Johannesson, E. Matzel, and S. P. Grand (2015), Evidence for long-lived subduction of an ancient tectonic plate beneath the southern Indian Ocean, *Geophys. Res. Lett.*, *42*, 9270–9278, doi:10.1002/2015GL066237.
Sliter, W. V. (1984), Foraminifers from Cretaceous limestone of the Franciscan Complex, northern California, in *Franciscan Geology of Northern California*, edited by M. C. Blake Jr., pp. 149–162, Society of Economic Paleontologists and Mineralogists, Pacific Section, Los Angeles, Calif.
Song, T. R. A., and D. Helmberger (2006), Low velocity zone atop the transition zone in the western US from *S* waveform triplication, in *Earth's Deep Water Cycle*, *Geophys. Monogr. Ser.*, vol. 168, edited by S. D. Jacobsen and S. Van Der Lee, pp. 195–213, AGU, Washington, D. C.
Song, T.-R. A., D. V. Helmberger, M. R. Brudzinski, R. W. Clayton, P. Davis, X. Perez-Campos, and S. K. Singh (2009), Subducting slab ultra-slow velocity layer coincident with silent earthquakes in southern Mexico, *Science*, *324*(5926), 502–506.
Spasojevic, S., L. Liu, and M. Gurnis (2009), Adjoint models of mantle convection with seismic, plate motion, and stratigraphic constraints: North America since the Late Cretaceous, *Geochem. Geophys. Geosyst.*, *10*, Q05W02, doi:10.1029/2008GC002345.
Sun, D., and D. Helmberger (2011), Upper-mantle structures beneath USArray derived from waveform complexity, *Geophys. J. Int.*, *184*(1), 416–438.
Sun, D., D. Helmberger, S. Ni, and D. Bower (2009), Direct measures of lateral velocity variation in the deep Earth, *J. Geophys. Res.*, *114*, B05303, doi:10.1029/2008JB005873.
Vallier, T. L., W. E. Dean, D. K. Rea, and J. Thiede (1983), Geologic evolution of Hess Rise, central North Pacific Ocean, *Geol. Soc. Am. Bull.*, *94*, 1289–1307.
van der Meer, D. G., W. Spakman, D. J. J. van Hinsbergen, M. L. Amaru, and T. H. Torsvik (2010), Towards absolute plate motions constrained by lower-mantle slab remnants, *Nat. Geosci.*, *3*, 36–40, doi:10.1038/ngeo708.
Zhong, S. J., and M. Gurnis (1995), Mantle convection with plates and mobile, faulted plate margins, *Science*, *267*(5199), 838–843.